Powder bed fusion electron beam of an oxygen-compatible β-Ti–35.5Nb–2Ta–3Zr alloy: Feasibility and material evaluation

(article starts on next page)

Powder bed fusion electron beam of an oxygen-compatible β-Ti–35.5Nb–2Ta–3Zr alloy: Feasibility and material evaluation

Silja-Katharina Rittinghaus, Sri Bala Aditya Malladi, Marcus Willi Rackel, Daniel Borchert, Hamed Shokri, Karin Ratschbacher, Michael Budnitzki, Bilal Gökce & Eduard Hryha

Published online: 11 Jan 2025.

Submit your article to this journal ⬈

Article views: 95

View related articles ⬈

View Crossmark data ⬈

Routledge
Taylor & Francis Group

OPEN ACCESS

Check for updates

Powder bed fusion electron beam of an oxygen-compatible β-Ti–35.5Nb–2Ta–3Zr alloy: Feasibility and material evaluation

Silja-Katharina Rittinghaus[a,b], Sri Bala Aditya Malladi[b], Marcus Willi Rackel[c], Daniel Borchert[a], Hamed Shokri[a], Karin Ratschbacher[d], Michael Budnitzki[e], Bilal Gökce[a] and Eduard Hryha[b]

aChair of Materials Science and Additive Manufacturing, School of Mechanical Engineering and Safety Engineering, University of Wuppertal, Wuppertal, Germany; bDepartment of Industrial and Materials Science, Chalmers University of Technology, Gothenburg, Sweden; cMetal Physics, Helmholtz-Zentrum Hereon, Geesthacht, Germany; dGfE Metalle und Materialien GmbH, Nürnberg, Germany; eInstitute for Advanced Simulations—Materials Data Science and Informatics (IAS-9), Forschungszentrum Jülich GmbH, Jülich, Germany

ABSTRACT

Additive manufacturing (AM) by powder bed fusion electron beam (PBF-EB) is a state-of-the-art method for processing titanium-based alloys, especially due to the high inherent oxygen affinity of the material. Ti–Nb–Ta–Zr alloys provide, dependent on composition and manufacturing, a versatile property profile and are of increasing interest as structural materials as AM eases their production. Enhancing sustainability through reduced purity requirements, alongside improved material performance, could lead to more efficient and environmentally-friendly material design. This study explores the feasibility of producing dense β-Ti–35.5Nb–2Ta–3Zr alloys with an elevated oxygen content of 2800 ppm through PBF-EB, achieving up to 99.7% density and notable mechanical properties such as a hardness of 330HV0.3. The microstructure was found to be single-β in all samples with low segregation of constitutional elements. Indications of a fibre texture switch, depending on the chosen process parameters, were found.

1. Introduction

Compared to (α + β) titanium alloys widely used in various applications, β-Ti alloys exhibit a number of unique properties, such as a low modulus of elasticity and high yield strength combined with excellent formability. In addition, these alloys also exhibit high mechanical strength, high fracture toughness and excellent resistance to stress corrosion cracking and hydrogen embrittlement (Achache et al., 2016; Bönisch et al., 2017; Obbard et al., 2010; Yuan et al., 2023). Research into β-Ti alloys increased considerably in recent years (da Silva et al., 2023). Among the β-Ti alloys, alloys based on quaternary Ti–Nb–Ta–Zr, so-called Ti–35.5Nb–2Ta–3Zr (TNTZ) alloys, also known as gum metals, are of particular interest. The alloy family was first described by Saito et al. (2003) and is characterized by a low modulus of elasticity of less than 70 GPa typical of the β-phase alloys, high tensile strength, superelasticity, and superplasticity at room temperature. Due to their excellent biocompatibility through the exclusive use of non-toxic and non-allergenic alloying elements in combination with the low modulus of elasticity, these new β-Ti alloys have interesting application prospects, particularly in the biomedical field (as stent or dental prosthesis material, etc.) (Nakai et al., 2009; Obbard et al., 2010; Stráský et al., 2017; Tahara et al., 2011).

In contrast to classic titanium alloys, a certain amount of oxygen in the solid solution is advantageous in gum alloys in order to achieve improved material properties. Oxygen contents between 0.7 and 3.0 at% (Talling et al., 2009) are reported, with 2000 ppm being cited as the minimum. The importance of oxygen for the properties and deformation mechanisms of gum metal is a widely studied variable, but there are still some contradictions. The addition of oxygen, like any other interstitial element, is responsible for an increase in mechanical strength as it causes solid solution hardening (Nakai et al., 2009; Stráský et al., 2017). In a recent investigation on a NbTiZr medium-entropy alloy (An et al., 2024), it was demonstrated that the addition of 1 at% oxygen resulted in a notable increase in the yield strength of the material manufactured by laser powder bed fusion (PBF-LB), emphasizing the potential of oxygen as an alloying element in refractory-based alloys. However, the influence of oxygen in β-Ti is complex, and some authors suggest that the addition of oxygen hinders the formation of α″ and ω phases, which play a fundamental role in the deformation mechanisms, since these phases strongly influence the elastic behaviour of β-Ti alloys (Besse et al., 2011; Tahara et al., 2011). Alloy concepts including oxygen, while enhancing specific mechanical attributes, may also decrease production costs due to higher tolerance for oxygen levels during processing, especially in additive manufacturing

(AM). The cost of raw materials could also decrease if lower purity materials can be used, potentially improving the economic feasibility for large-scale industrial production. However, the reproducibility of the desired oxygen concentration and the associated microstructural characteristics across larger batches and varied production environments presents a potential challenge, especially given the difficulty in achieving the desired mechanical properties for TNTZ.

The target properties of TNTZ are typically achieved when a strong mechanical cold working of about 90% area reduction takes place during the processing of these alloys (Furuta et al., 2005; Saito et al., 2003). In general, cold working reduces the modulus of elasticity and increases the yield strength. In view of these aspects, the requirement for processing these materials is usually a high degree of plastic deformation (Saito et al., 2003). Gum metal is therefore usually produced by powder metallurgy or by arc melting with subsequent plastic deformation. These manufacturing routes are comparatively complex, especially for the production of filigree components, which is the motivation for the use of AM.

It has been shown that gum metal can be successfully processed by AM. Batalha et al. employed a β-TNTZ alloy (Ti–35Nb–5Ta–7Zr) for PBF-LB and demonstrated excellent mechanical properties in compression tests, exhibiting a modulus of elasticity of around 45 GPa. Moreover, biocompatible implants were manufactured as prototypes in the study, thereby providing successful proof of the filigree components (Batalha et al., 2020). The authors found columnar grain growth, which is typical for AM and is aligned in the direction of construction, which was associated with the anisotropy of the mechanical properties that were also observed. The same research group successfully fabricated oligocrystalline structures with a combination of PBF-LB and heat treatment (Batalha et al., 2020), which exhibited significantly increased strength compared to untreated material, which was partly attributed to oxygen uptake during heat treatment. With regard to the production of biocompatible metal implants, Xu et al. (2022) investigated the scanning strategy and corrosion properties in 3.5 wt% NaCl solution of Ti–35Nb–2Ta–3Zr–0.3O produced by PBF-LB. Nadammal et al. (2022) investigated the influence of volume energy densities in an additively manufactured by PBF-LB Ti–35Nb–7Zr–5Ta. They reported that higher values for the energy densities led to higher mechanical strengths with a slight decrease in ductility. A cellular to dendritic solidification morphology was observed in the processed samples. Lower niobium concentrations were also investigated. Luo et al. (2019) performed promising cell proliferation tests on Ti–30Nb–5Ta–3Zr (PBF-LB). They also found that stress relieve heat treatment at 600 °C for 3 hrs promoted the formation of α-needles. In a different study (Luo et al., 2021),

PBF-LB of Ti–34.2Nb–6.8Zr–4.9Ta–2.3Si was investigated with a focus on processing parameters. The researchers achieved high densities (99.7%) and reported on different Si-containing intermetallic phases in the solids. Yang et al. (2020) were the first group to publish on powder bed fusion electron beam (PBF-EB) of a TNTZS alloy (Ti–35Nb–5Ta–7Zr–2Si). PBF-EB is particularly well-suited for the production of TNTZ alloys due to its ability to operate in a high-vacuum environment, which minimizes oxygen contamination—crucial for maintaining the alloy's unique mechanical properties. They also focused on post heat treatment, and reported a compressive yield strength of 791.15 ± 23.17 MPa, an elastic modulus of 67.82 ± 3.06 GPa and a ductility of $48.22 \pm 0.9\%$ after heat treatment at 1000 °C for 2 h followed by water quenching. Their study thus provided valuable input for developing processing parameters in our own work. The work by Hafeez et al. (2019) on PBF-LB of Ti–35Nb–2Ta–3Zr–0.12O is also of particular interest as per the similarity of the used alloy. The authors focused on cyclic loading–unloading tests on as-built samples and extensive high-resolution transmission electron microscopy (HRTEM) investigation with special regard to stress-induced phase transformation and deformation. The measured recoverable strain (4.8% at 27% deformation) outlines the prospective capabilities of additive manufactured TNTZ.

In this work, we investigate the manufacturing of dense solid samples out of Ti–35.5Nb–2Ta–3Zr–0.28O by PBF-EB in vacuum. The resulting microstructure and hardness are investigated and correlated with build parameters. It is assumed that within the process window for dense samples, the microstructure can be specifically influenced by the selected process parameters. In perspective, this points the way towards locally customizable properties, one of the main advantages of AM.

2. Experimental (method and material)

2.1. Material

The powder material (Figure 1) with the nominal composition 59.05Ti–35.55Nb–2.96Zr–2.0Ta (wt%) and 0.28 wt% O was produced by GfE Metalle und Materialien GmbH using electrode inert gas atomization (EIGA) with D10 = 60 μm, D50 = 100 μm and D90 = 165 μm after sieving (Figure 1(c)). The particles appear predominantly spherical in shape (Figure 1(a)), occasional gas inclusions are visible upon the analysis of particle cross sections (Figure 1(b)), origination from the atomization process. Irregular shaped chunks interpreted to be incompletely dissolved mixed refractory metals can occasionally be observed. The substrate material used for all samples was Ti6Al4V with as-milled surface.
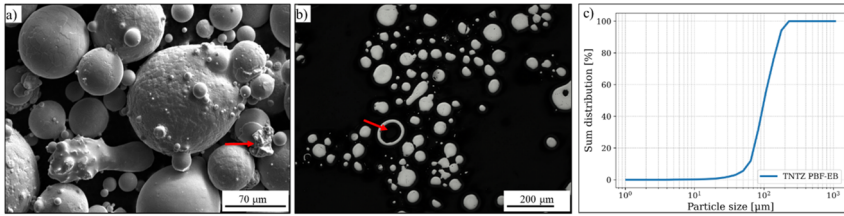
Figure 1. Powder material used in this study: SEM imaging (a), light optical microscopy (LOM) imaging of cross sections (b), results of particle size measurement by means of laser diffraction (c) using a Helos/Br+Oasis/L+Vibri/L (Sympatec) device. Red arrows indicate remaining chunks of presumable refractory metals (a) and gas inclusions (b) respectively.
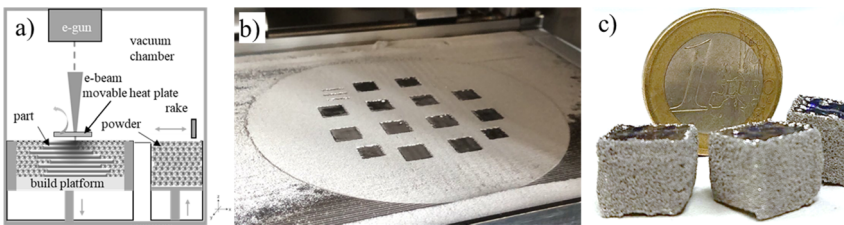

Figure 2. Schematic PBF-EB process (a), produced cubic samples of $10\times10\times10\,mm^3$ size (b) inside the machine and (c) after depowdering.

2.2. Manufacturing

For PBF-EB manufacturing of samples, a Freemelt ONE electron beam powder bed fusion machine was used. In Figure 2, the setup is depicted schematically. To diminish the risk of smoke events, preheating and sintering were done indirectly by radiation from an electron beam heated carbon plate close above the powder bed. As a geometry, cubic volumes of 10 mm edge length were built. Results of one exemplary build job are presented to document the part (Figure 2(b)) and surface quality (Figure 2(c)) respectively.

Process parameters applied in this study are depicted in Figure 3. Both line offset Δy_s and layer offset D_L were set to be 0.1 mm with a track width of approximately 0.25 mm. The preheating temperature was held constant at 650 °C during each respective build. A layer wise 90° rotated, bidirectional stripe pattern was applied as a scanning strategy. The line energy E_L is given according to $E_L = P_{EB}/v_s$ with P_{EB} = electron beam power and v_s = scan speed. Currents of 12, 15, and 20 mA were used, while the voltage was 60 kV. For clearer representations, the unit Watt (W) as the multiplication product is used in the following. No contour scan was applied, as can also be seen from the rough surface of the samples depicted in Figure 2(c).
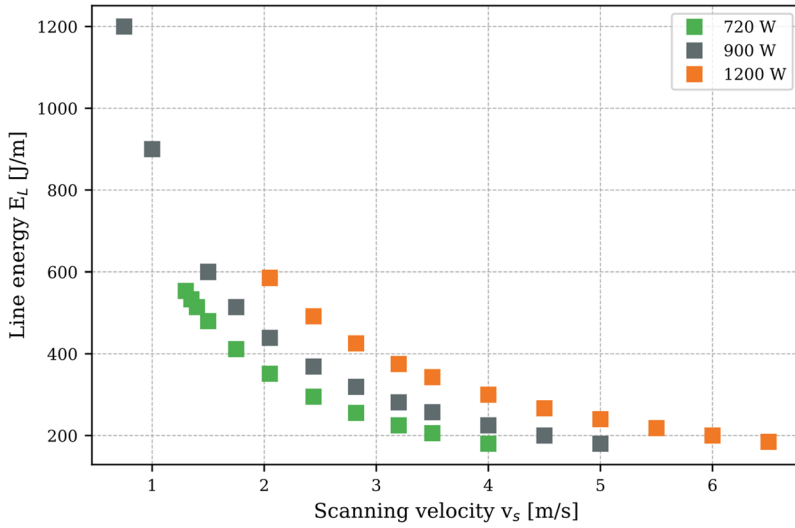
Figure 3. PBF-EB processing parameters applied in this study.

2.3. Material characterization

All samples were cut and metallographically prepared parallel to the build direction to create x–z cross sections. For density and hardness measurements, the samples were analysed in standard polished surface condition. The density was determined by optical analysis, using a Leica DM2700 for light microscopy imaging and ImageJ 1.53. for quantification. For each sample, one complete cross section was measured, so that no error bars are included in the visualization of the measurements. Scanning electron microscopy (SEM) imaging has been done using a Zeiss Gemini 450. For electron backscatter diffraction (EBSD), the sample's surfaces were additionally polished using oxide polishing suspension (OP-S). The detector for EBSD was an Oxford symmetry, and measurements were performed at 20 keV acceleration voltage and 15 nA current. Data analysis was done using the opensource MATLAB tool MTEX on maps obtained by AZtec software (Oxford Instruments). The detector used for energy dispersive X-ray spectrometry (EDS) was an Oxford Ultim Max. High-energy X-ray experiments were conducted at the Hereon run beam line HEMS (High Energy Materials Science) at PETRA III at the Deutsches Elektronen-Synchrotron (DESY), Hamburg, Germany (Schell et al., 2013; Staron et al., 2011). The specimens were measured in transmission with a beam size of 1 mm by 1 mm and a photon energy of 100 keV ($\lambda = 0.1240$ Å). During the High-energy X-ray diffraction (HEXRD) experiments, the Debye–Scherrer diffraction rings were recorded on a Perkin Elmer XRD 1622 flat panel detector. In order to calibrate the instrument, a measurement was conducted with a standardized lanthanum hexaboride (LaB6) powder, which

was used to calculate the instrumental parameters, the beam centre, and the sample-detector distance. The diffraction rings were integrated azimuthally using the Fit2D software package (Hammersley, 1997; Hammersley et al., 1996), and phase fractions were calculated with the Rietveld analysis software package MAUD (Lutterotti, 2010). Micro-hardness measurements on all samples were performed using an ATM Qness Carat 930 Vickers hardness tester with measuring minimum 10 indents parallel to the build direction each. Samples with low density were excluded from this type of investigation. The chemical composition of powder and consolidated material was determined by X-ray fluorescence (XRF, main elements), inductively coupled plasma spectrometry (ICP), and carrier gas hot extraction analysis (CGHE, O).

3. Results

3.1. Macroscopic properties

3.1.1. Relative density and defects

In Figure 4, an overview of the achieved relative densities in relation to the applied line energy which is directly related to the respective scanning velocity is depicted. It can be derived that for nearly dense samples (>99.0%) at least 370 J/m, or 37 J/mm^3, are required. The width of the processing window regarding scanning speeds is thus being observed to be similar for
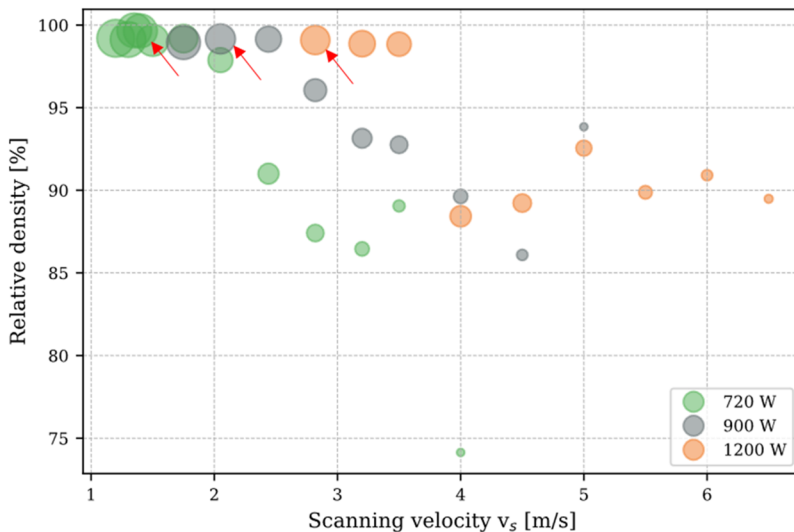

Figure 4. Relative densities determined in dependence of processing parameters. Data point sizes indicate the value of E_L on a relative scale, ranging from 180 J/m (min. size) to 1200 J/m (max. size) for easier correlation with Figure 3. Red arrows mark the samples selected for microstructural investigation.
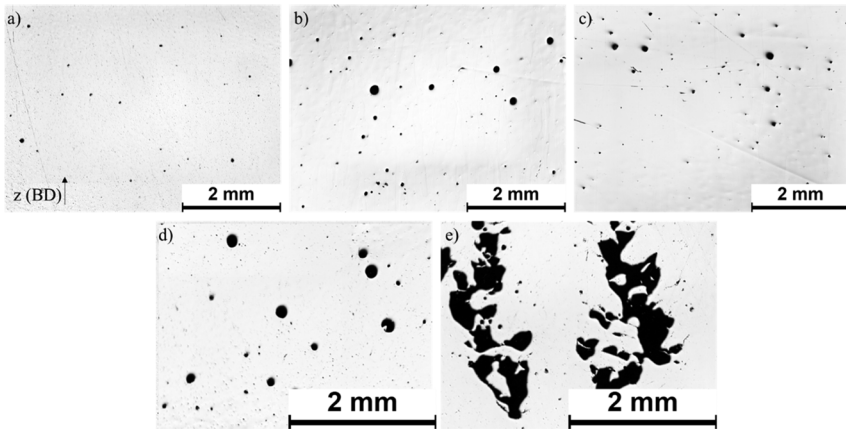
Figure 5. Light microscopy images of PBF-EB processed samples at: (a) 720 W (BD = build direction), (b) 900 W, and (c) 1200 W electron beam power. Typical defects observed in this study: (d) pores (720 W, 1.5 m/s) and (e) lack of fusion (LoF, 720 W, 3.2 m/s).

all tested electron beam energies; however, highest densities of over 99.5% were achieved for 720 W. Light microscopic images (Figure 5(a–c)) provide an overview of the respective samples with highest densities per electron beam power, which are also marked by red arrows in Figure 4.

Typical defects when exceeding the parameter range for dense samples are depicted in Figure 5(d,e). An excess in energy, resulting from a relatively slow scanning speed or increased applied energy, leads to higher porosity. This occurs due to overheating, which can cause vaporization of the material and entrap gas during solidification. Additionally, the comparatively large melt pools caused by the high layer thickness of 100 μm further promote entrapment of gas, either previously dissolved or enclosed in powder particles. Lack of fusion (Figure 5(e)), on the other hand, indicates insufficient energy to achieve complete melting and bonding between layers, and this defect is consistently observed in samples built with low energy densities. While not relevant in this case, similar defects can also arise from issues with powder deposition or unsuitable scanning strategies.

3.1.2. Microhardness

For microhardness measurements (HV0.3), samples with a density <98.0% were neglected. The results (Figure 6) show almost no significant differences between the averaged hardness values of the samples. A clear distinction between the 900 and 720 W samples cannot be established due to the significant margin of error, which can be attributed to the observed porosity (Figure 5) causing high scatter. However, a significant decrease in
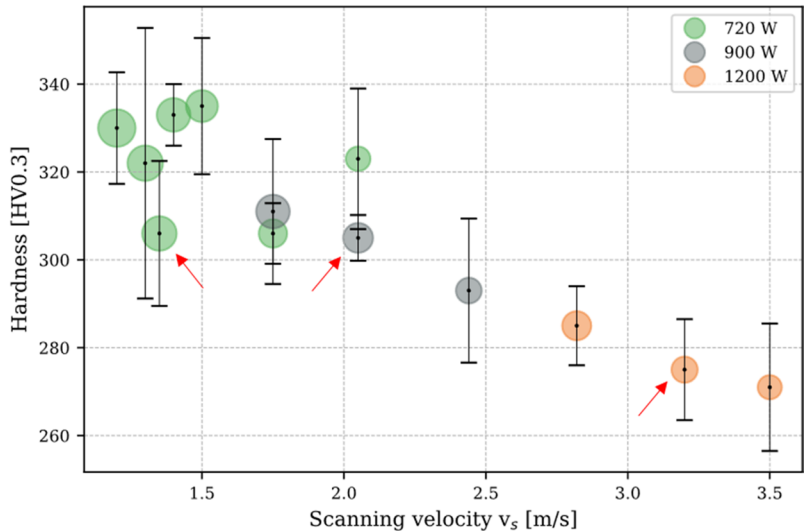
Figure 6. Microhardness plotted over scanning velocity. Data point sizes indicate the value of E_L on a relative scale, ranging from 180 J/m (min. size) to 1200 J/m (max. size) for easier correlation with Figures 3 and 4 (identical scale). Red arrows mark the samples selected for microstructural investigation.

Table 1. Chemical composition determined by XRF and CGHE.

Composition (wt%)	Ti	Nb	Zr	Ta	O
Powder material	59.05	35.55	2.96	2.02	0.28
PBF-EB bulk sample[a]	59.10	35.55	2.96	2.01	0.27

[a]Build parameters: $P_{EB}=720$ W and $v_s=1.35$ mm/s.

hardness for 1200 W (high scanning velocity) samples compared to 720 W (low scanning velocity) samples with the latter exhibiting about 15% higher values was observed.

3.1.3. Chemical composition

The chemical composition (Table 1) remains nearly constant during the build. The slight decrease in oxygen can be attributed to deoxidation in vacuum (Ono & Moriyama, 1982), which is rather low particularly because of high Ti and Zr contents. With oxygen being a crucial alloying element (Stráský et al., 2017), its tracking is essential for TNZT alloys.

3.2. Microstructure

3.2.1. Grain characteristics and texture

The microstructure of the material in Figure 7(a–c) consists of similar epitaxially grown, columnar grains, while the pattern resulting from layer
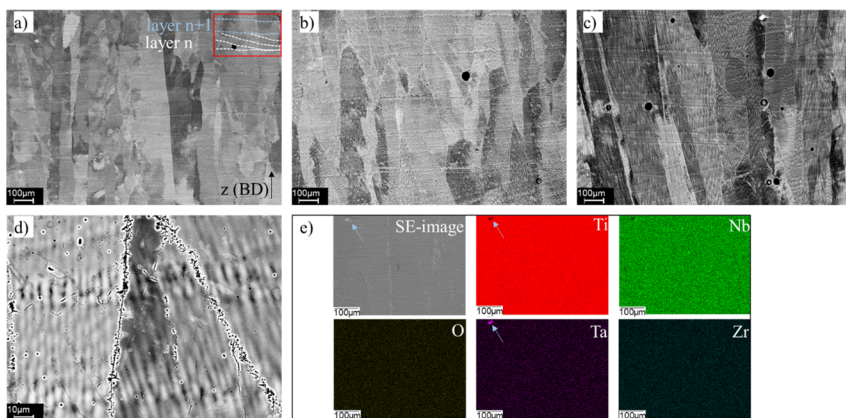
Figure 7. Microstructures revealed by SEM of etched samples (Kroll): (a) 720 W (BD = build direction), (b) 900 W, (c) 1200 W electron beam energy, (d) close up of grain boundaries, and (e) EDS compositional mapping for the main elements (720 W sample). Corresponding EDS measurement results are O = 3.12 ± 0.03, Ti = 58.2 ± 0.06, Nb = 33.51 ± 0.05, Zr = 2.97 ± 0.04, Ta = 2.19 ± 0.06 (in wt%). The inset in (a) illustrates exemplarily the tracks of two subsequent layers, in order to highlight the size relationships in comparison to the image section.

wise change of the scan direction remains visible as marked (Figure 7(a), red rectangle). While layer n is cut perpendicular to the scan direction and is thus shown in the y–z plane, the subsequent layer $n+1$ is cut parallel to the scan direction and is depicted in the x–z plane. Upon closer observation (Figure 7(d)), the cellular morphology inside the grains becomes evident; most clearly seen at the lower melt track boundaries. The composition obtained from EDS analysis (Figure 7(e), table) of the investigated sample (720 W) closely matches the chemical composition determined by full chemical analysis. The compositional maps for Ti and Nb indicate that the sample is predominantly chemically homogeneous, with no noticeable segregation. However, isolated inclusions are observed, also visible in the SEM image, which are identified as being highly Ta-rich according to the analysis. For the other elements, no anomalies are observed. It is worth noting that the signals for Ta, Zr, and O are generally quite weak, as also indicated by the fact that the Ta inclusion is not visible in the Zr and O maps. However, due to the good solubility of both elements, and especially considering the homogeneous distribution of Nb, an overall homogeneous distribution can be assumed.

Figure 8 reveals grain sizes and morphologies as well the crystallographic textures of the samples analysed by EBSD. While the latter is mostly (001) for all samples, it is strongest for the material produced with 1200 W electron beam power. The texture in both 720 and 900 W produced samples is visibly weaker, while especially in the 720 W sample, in
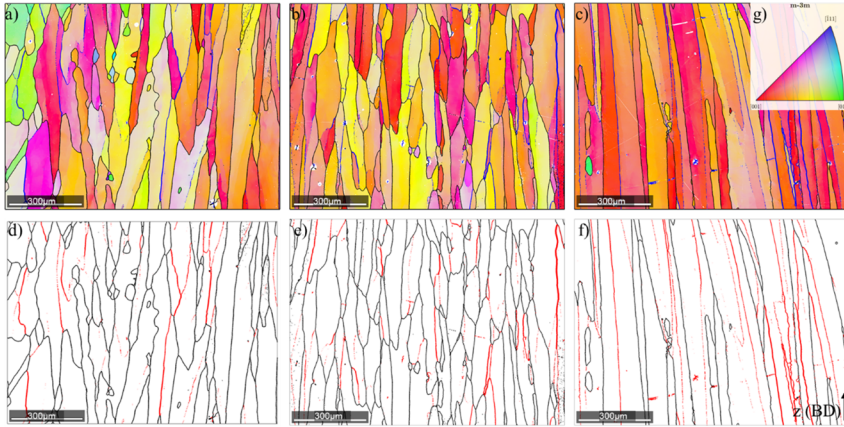
Figure 8. EBSD results for (a,d) 720 W, (b,e) 900 W, and (c,f) 1200 W electron beam power with (a–c) representing invese pole figure (IPF) colour maps in *y*-direction according to the key depicted as inset (g) in (c), and corresponding visualization of grain boundaries with black lines indicating high-angle (>10°) and red lines low-angle (≤10°) grain boundaries, respectively (BD = build direction). Whitish areas in (a–c) can be attributed to porosity and remaining artefacts from preparation.
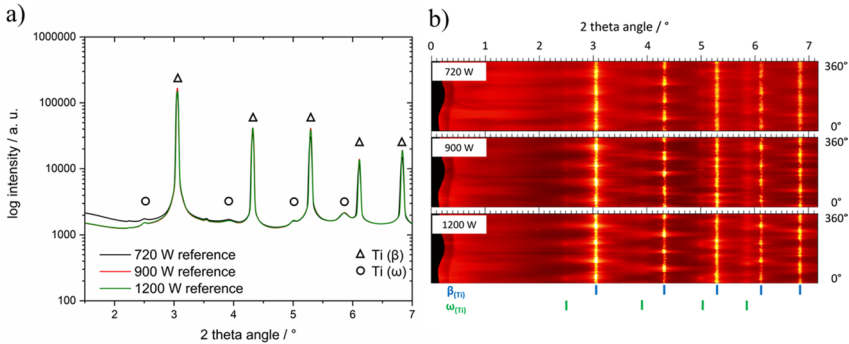
Figure 9. XRD results for samples built with 720, 900, and 1200 W electron beam power; (a) diffraction patterns with associated phases and (b) colour-coded XRD patterns (original graph) with indicated phase positions.

parts, a mixture of (011)/(111) crystallographic orientation of the grains can also be observed. The structure of all resolved grains was found to be bcc (β-Ti). No significant difference in the amount of low-angle sub-grain boundaries was observed.

3.2.2. Phase composition

The three selected TNTZ samples, with their respective build parameters referring to $P_{EB} = 720$, 900, and 1000 W, exhibit an almost single-phase appearance. In all three samples, the majority phase is the Ti(β) phase (Figure 9).

Table 2. Phase fractions and lattice parameters of as-built PBF-EB samples.

Electron beam power (P_{EB})	Ti (α)	Ti (β)		ω
		a (Å)	Phase fraction (%)	
720 W	No	3.2910	≈100.0	0–1%
900 W	No	3.2877	≈100.0	0–1%
1000 W	No	3.2881	≈100.0	0–1%

The lattice parameters differ only slightly from each other (Table 2). It is evident that the different energies used do not significantly influence the lattice parameters of the as-built states. All samples also show signs of the ω phase. Their peak intensity is very low, combined with a large peak width. This is indicative of small, very finely dispersed ω phase particles. The exact phase fraction cannot be accurately determined from the appearance and low peak intensity. An estimate based on the peak intensities gives a phase fraction <1%.

4. Discussion

The challenging process of atomization of a high refractory metal containing alloy has been successful in terms of producing material of appropriate size distribution and flowability. However, the isolated inclusions found in the consolidated samples suggest that a small fraction of the pre-material, particularly Ta due to its high melting point, was not dissolved homogeneously. This observation is consistent with the findings in Pereira et al. (2022), where the stepwise sintering of a TNTZ alloy and the increasing dissolution of the high-temperature elements were investigated. A promising approach for further homogenization of the powder could be the optimization of the atomization process. In particular, the atomization of electrodes made of master alloys and pure elements with the EIGA process requires longer dwell times at the electrode tip to enable a sufficient alloying time. Couret et al. (2021) demonstrated that reducing the deposition rate resulted in a significant improvement in homogeneity in a TiAl alloy containing tungsten. In terms of the homogeneity of the PBF-EB material, the high processing temperatures might be of interest, as they effectively act as an in-situ heat treatment. However, it is also clear that 600 °C is not sufficient to fully dissolve the high-melting elements. Therefore, any fragments or powder particles must be sufficiently small to ensure complete melting during the process, and a high level of homogeneity in the starting material is also essential. According to the compositional maps, this was almost fully achieved.

The determined process parameter range for samples of high density is in good accordance with the information from Yang et al. (2020), where highest densities were reportedly achieved with line energies of

approximately 200–300 J/m for Ti–35Nb–5Ta–7Zr for a 30% smaller layer offset of 0.07 mm, translating to approximate volume energy densities of 30-45 J/mm³. Highest densities achieved in this study were about 99.7%, which is expected to be further reduced when smaller layer heights are selected. The observed epitaxial growth of columnar grains is typical for especially additively manufactured materials built with high process energies and low layer wise variation (here: 90°) of the scan vector orientation. Thus, further grain size variation is prospectively expected to be enabled by more complex line scan strategies, characterized by the length, orientation, and sequence of the scan vectors, while new degrees of freedom can also be realized by spot melting strategies, as we described in, for example, Rittinghaus et al. (2023). While samples produced in previous studies by Yang et al. (2020) showed a weak metallographic texture, in our work a strong (001) texture was determined for all but specifically high-energy produced samples. This is also typical for PBF-EB, it is interesting though that in some regions of the 720 W produced samples also grains with mixed (011)/(011) orientation can be recognized, which indicates great possibilities for targeted texture design. Similar observations of fibre texture switch were also made in PBF-EB of, for example, molybdenum (Fernandez-Zelaia et al., 2021) and tungsten (Ledford et al., 2023) with experimentally being correlated with decreasing beam current and scan velocity. Is has been assumed in the aforementioned literature that the evolution of the weld pool shape governs the fibre selection. However, the mechanism behind the switching phenomena has not yet been clearly elucidated. Fernandez-Zelaia et al. (2021) found a similar correlation between PBF-EB processing and the presence of low-angle grain boundaries, possibly indicating different levels of stress to which the material was subjected during processing. In the present study on TNTZ, we could not observe this effect. However, unlike the mentioned study, the energy densities were very similar here, combined with high processing temperatures, suggesting that the stresses hypothesized as the cause in the other study were likely to be comparatively low in our case.

For the alloy investigated in this study, both grain boundary hardening according to the Hall–Petch relation (Hall, 1934) and possible phase transformations, specifically the formation of α-phase, were considered to contribute to the materials hardness. The material was found to be predominantly in the β phase, with EBSD measurements showing visible microstructural differences between the samples at 750 and 900 W as compared to those processed at 1200 W. The lower hardness values in the latter samples can be attributed to increased grain size. However, a clear correlation with the classic Hall–Petch relationship could not be confirmed; this can in part be attributed to the large uncertainty in the hardness value at 750 W, but is also indicative of additional factors that influence hardness.

Refractory metal inclusions from the atomization process may contribute to hardening, though SEM analysis did not reveal a quantitatively significant presence of these oxygen-rich phases. Further, the presence of retained fine particles, such as high-melting-point metal clusters (e.g., Ta), may contribute to the higher hardness values observed in samples processed with lower local energies; higher energy input, resulting in higher processing temperatures, promotes the dissolution of these inhomogeneities, and facilitates dislocation annihilation reducing their impact on the mechanical properties. To investigate these hypotheses, further studies using high-resolution analytical techniques, such as TEM or atom probe tomography (APT), are required. Furthermore, higher process temperatures promote the dislocation annihilation. However, it should be noted that the material studied here may also undergo athermal stress-induced phase transformations (Zhang et al., 2017). As these are reversible, they were not possible to be investigated with the methods being available for this study, nevertheless, this might be considered a worthy subject for future in-situ studies especially in combination with further investigation on thermal phase transformations of the metastable material. Investigating the impact of varying oxygen contents is also of significant interest. For example, in biomedical implants, the oxygen content may influence the material's corrosion resistance and biocompatibility, potentially affecting its long-term performance within the human body. Therefore, while the initial properties of PBF-EB-manufactured TNTZ alloys are promising, a more in-depth study of these factors is essential to fully evaluate their potential for real-world applications.

5. Conclusions

In this study, prealloyed TNTZ powder produced by EIGA was processed via PBF-EB, and the resulting components were analysed for microstructural characteristics. The findings indicate a broad processing window that allows for the production of defect-free samples with low porosity (<0.3%). The chosen parameters significantly influenced the initial hardness of the material, which ranged from approximately 270 to 340 HV0.3. This variation in hardness was primarily, though not exclusively, linked to differences in grain size. Further, the parameters had a mild effect on the texture, suggesting potential for targeted microstructure optimization. The material largely consisted of a single β phase after processing, with no premature heat treatment effects observed from the elevated processing temperatures. The controlled oxygen content achieved through vacuum processing offers promising opportunities for oxygen-compatible TNTZ alloys in medical and structural applications, particularly given the successful production of prealloyed, atomized powders containing

high-melting refractory metals. Future work will focus on more detailed microstructural analysis and explore methods for tailoring microstructures and mechanical properties through suitable post-processing techniques. Of specific interest is the determination of the elastic modulus and in-depth investigation of the expected superelastic behaviour.

Acknowledgements

CRediT author statement

Silja-Katharina Rittinghaus: Conceptualization, investigation, visualization, writing—original draft preparation. *Sri Bala Aditya Malladi:* Investigation, visualization, writing—reviewing and editing. *Marcus Willi Rackel:* Resources, investigation, writing—original draft preparation. *Daniel Borchert:* Investigation. *Hamed Shokri:* Investigation. *Karin Ratschbacher:* Investigation. *Michael Budnitzki:* Writing—reviewing and editing. *Bilal Gökce:* Resources, writing—reviewing and editing. *Eduard Hryha:* Resources, writing—reviewing and editing.

Disclosure statement

The authors declare that they have no known competing financial interests or personal relationships that could have appeared to influence the work reported in this paper.

Funding

References

Achache, S., Lamri, S., Alhussein, A., Billard, A., François, M., & Sanchette, F. (2016). Gum Metal thin films obtained by magnetron sputtering of a Ti-Nb-Zr-Ta target. *Materials Science and Engineering: A*, *673*, 492–502. https://doi.org/10.1016/j.msea.2016.07.096

An, Y., Liu, Y., Liu, S., Zhang, B., Yang, G., Zhang, C., Tan, X., Ding, J., & Ma, E. (2024). Additive manufacturing of a strong and ductile oxygen-doped NbTiZr

medium-entropy alloy. *Materials Futures, 4,* 015001. https://doi.org/10.1088/2752-5724/ad8df2

Batalha, R. L., Batalha, W. C., Deng, L., Gustmann, T., Pauly, S., Kiminami, C. S., & Gargarella, P. (2020). Processing a biocompatible Ti–35Nb–7Zr–5Ta alloy by selective laser melting. *Journal of Materials Research*, *35*(9), 1143–1153. https://doi.org/10.1557/jmr.2020.90

Batalha, R. L., Pauly, S., Kühn, U., Kosiba, K., Bolfarini, C., Kiminami, C. S., & Gargarella, P. (2020). Oligocrystalline microstructure in an additively manufactured biocompatible Ti-Nb-Zr-Ta alloy. *Materials Letters*, *262*, 127149. https://doi.org/10.1016/j.matlet.2019.127149

Besse, M., Castany, P., & Gloriant, T. (2011). Mechanisms of deformation in gum metal TNTZ-O and TNTZ titanium alloys: A comparative study on the oxygen influence. *Acta Materialia*, *59*(15), 5982–5988. https://doi.org/10.1016/j.actamat.2011.06.006

Bönisch, M., Panigrahi, A., Stoica, M., Calin, M., Ahrens, E., Zehetbauer, M., Strotzki, W., & Eckert, J. (2017). Giant thermal expansion and α-precipitation pathways in Ti-alloys. *Nature Communications*, *8*(1), 1429. https://doi.org/10.1038/s41467-017-01578-1

Couret, A., Allen, M., Rackel, M. W., Galy, B., Monchoux, J.-P., Güther, V., Pyczak, F., Sallot, P., & Thomas, M. (2021). Chemical heterogeneities in tungsten containing TiAl alloys processed by powder metallurgy. *Materialia*, *18*, 101147. https://doi.org/10.1016/j.mtla.2021.101147

da Silva, M. R., Plaine, A. H., Pinotti, V. E., Mazzer, E. M., & Bolfarini, C. (2023). A review of gum metal: Developments over the years and new perspectives. *Journal of Materials Research*, *38*(1), 96–111. https://doi.org/10.1557/s43578-022-00781-1

Fernandez-Zelaia, P., Ledford, C., Ellis, E. A. I., Campbell, Q., Rossy, A. M., Leonard, D. N., & Kirka, M. M. (2021). Crystallographic texture evolution in electron beam melting additive manufacturing of pure molybdenum. *Materials and Design*, *207*, 109809. https://doi.org/10.1016/j.matdes.2021.109809

Furuta, T., Kuramoto, S., Hwang, J., Nishino, K., & Saito, T. (2005). Elastic deformation behavior of multi-functional Ti–Nb–Ta–Zr–O alloys. *Materials Transactions*, *46*(12), 3001–3007. https://doi.org/10.2320/matertrans.46.3001

Hafeez, N., Liu, S., Lu, E., Wang, L., Liu, R., Lu, W., & Zhang, L.-C. (2019). Mechanical behavior and phase transformation of β-type Ti-35Nb-2Ta-3Zr alloy fabricated by 3D-Printing. *Journal of Alloys and Compounds*, *790*, 117–126. https://doi.org/10.1016/j.jallcom.2019.03.138

Hall, E. O. (1934). The deformation and aging of mild steel: III. Discussion of results. *Proceedings of the Royal Society A*, *143*, 499–527.

Hammersley, A. P. (1997). *FIT2D: An introduction and overview* (ESRF Internal Report).

Hammersley, A. P., Svensson, S. O., Hanfland, M., Fitch, A. N., & Hausermann, D. (1996). Two-dimensional detector software: from real detector to idealised image or two-theta scan. *High Pressure Research*, *14*(4–6), 235–248. https://doi.org/10.1080/08957959608201408

Ledford, C., Fernandez-Zelaia, P., Graening, T., Campbell, Q., Rojas, J. O., Rossy, A. M., Kato, Y., & Kirka, M. M. (2023). Microstructure and high temperature properties of tungsten processed via electron beam melting additive manufacturing. *International Journal of Refractory Metals and Hard Materials*, *113*, 106148. https://doi.org/10.1016/j.ijrmhm.2023.106148

Luo, J. P., Sun, J. F., Huang, Y. J., Zhang, J. H., Zhang, Y. D., Zhao, D. P., & Yan, M. (2019). Low-modulus biomedical Ti–30Nb–5Ta–3Zr additively manufactured by selective laser melting and its biocompatibility. *Materials Science & Engineering. C, Materials for Biological Applications*, 97, 275–284. https://doi.org/10.1016/j.msec.2018.11.077

Luo, X., Yang, C., Fu, Z. Q., Liu, L. H., Lu, H. Z., Ma, H. W., Wang, Z., Li, D. D., Zhang, L. C., & Li, Y. Y. (2021). Achieving ultrahigh-strength in beta-type titanium alloy by controlling the melt pool mode in selective laser melting. *Materials Science and Engineering: A*, 823, 141731. https://doi.org/10.1016/j.msea.2021.141731

Lutterotti, L. (2010). Total pattern fitting for the combined size-strain-stress-texture determination in thin film diffraction. *Nuclear Instruments and Methods in Physics Research Section B: Beam Interactions with Materials and Atoms*, 268(3–4), 334–340. https://doi.org/10.1016/j.nimb.2009.09.053

Nadammal, N., Rajput, M., Gupta, S. K., Ivanov, E., Reddy, A. S., Suwas, S., & Chatterjee, K. (2022). Laser powder bed fusion additive manufacturing of a low-modulus Ti–35Nb–7Zr–5Ta alloy for orthopedic applications. *ACS Omega*, 7(10), 8506–8517. https://doi.org/10.1021/acsomega.1c06261

Nakai, M., Niinomi, M., Akahori, T., Tsutsumi, H., & Ogawa, M. (2009). Effect of oxygen content on microstructure and mechanical properties of biomedical Ti-29Nb-13Ta-4.6Zr alloy under solutionized and aged conditions. *Materials Transactions*, 50(12), 2716–2720. https://doi.org/10.2320/matertrans.MA200904

Obbard, E. G., Hao, Y. L., Akahori, T., Talling, R. J., Niinomi, M., Dye, D., & Yang, R. (2010). Mechanics of superelasticity in Ti–30Nb–(8–10)Ta–5Zr alloy. *Acta Materialia*, 58(10), 3557–3567. https://doi.org/10.1016/j.actamat.2010.02.010

Ono, K., & Moriyama, J. (1982). Deoxidation of high-melting-point metals and alloys in vacuum. *Metallurgical Transactions B*, 13(2), 241–249. https://doi.org/10.1007/BF02664581

Pereira, R. M., Koga-Ito, C. Y., Rovetta, S. M., Oliveira, M. A. C., Sampaio, A. G., Lima, G. M. G., & Henriques, V. A. R. (2022). Bone tissue engineering: production of TNTZ alloy by powder metallurgy. *Bone Research*, 12(2), 1526–1546. https://doi.org/10.33263/BRIAC122.15261546

Rittinghaus, S.-K., Shokri, H., Shkodich, N., Bruder, E., Farle, M., & Gökce, B. (2023). Comparative insights into microstructure and magnetism of Ni-Mn-Sn Heusler alloys manufactured by electron beam and laser beam powder bed fusion. *Additive Manufacturing Letters*, 7, 100159. https://doi.org/10.1016/j.addlet.2023.100159

Saito, T., Furuta, T., Hwang, J. H., Kuramoto, S., Nishino, K., Suzuki, N., Chen, R., Yamada, A., Ito, K., Seno, Y., Nonaka, T., Ikehata, H., Nagasako, N., Iwamoto, C., Ikuhara, Y., & Sakuma, T. (2003). Multifunctional alloys obtained via a dislocation-free plastic deformation mechanism. *Science*, 300(5618), 464–467. https://doi.org/10.1126/science.1081957

Schell, N., King, A., Beckmann, F., Fischer, T., Müller, M., & Schreyer, A. (2013). The high energy materials science beamline (HEMS) at PETRA III. *Materials Science Forum*, 772, 57–61. https://doi.org/10.4028/www.scientific.net/MSF.772.57

Staron, P., Fischer, T., Lippmann, T., Stark, A., Daneshpour, S., Schnubel, D., Uhlmann, E., Gerstenberger, R., Camin, B., Reimers, W., Eidenberger, E., Clemens, H., Huber, N., & Schreyer, A. (2011). In situ experiments with synchrotron high-energy X-rays and neutrons. *Advanced Engineering Materials*, 13(8), 658–663. https://doi.org/10.1002/adem.201000297

Stráský, J., Harcuba, P., Václavová, K., Horváth, K., Landa, M., Srba, O., & Janeček, M. (2017). Increasing strength of a biomedical Ti-Nb-Ta-Zr alloy by alloying with Fe, Si and O. *Journal of the Mechanical Behavior of Biomedical Materials*, *71*, 329–336. https://doi.org/10.1016/j.jmbbm.2017.03.026

Tahara, M., Kim, H. Y., Inamura, T., Hosoda, H., & Miyazaki, S. (2011). Lattice modulation and superelasticity in oxygen-added β-Ti alloys. *Acta Materialia*, *59*(16), 6208–6218. https://doi.org/10.1016/j.actamat.2011.06.015

Talling, R. J., Dashwood, R. J., Jackson, M., & Dye, D. (2009). On the mechanism of superelasticity in gum metal. *Acta Materialia*, *57*(4), 1188–1198. https://doi.org/10.1016/j.actamat.2008.11.013

Xu, H., Li, Z., Dong, A., Zhao, Y., Zhang, T., Xing, H., & Sun, B. (2022). Investigation on the effect of scanning strategy on the corrosion properties of gum metal produced using selective laser melting. *Materials Characterization*, *189*, 111929. https://doi.org/10.1016/j.matchar.2022.111929

Yang, K., Wang, J., Tang, H., & Li, Y. (2020). Additive manufacturing of in-situ reinforced Ti–35Nb–5Ta–7Zr (TNTZ) alloy by selective electron beam melting (SEBM). *Journal of Alloys and Compounds*, *826*, 154178. https://doi.org/10.1016/j.jallcom.2020.154178

Yuan, S., Lin, N., Zeng, Q., Zhang, H., & Wu, Y. (2023). Recent advances in gum metal: Synthesis, performance and application. *Critical Reviews in Solid State Material Science*, *48*(2), 257–288. https://doi.org/10.1080/10408436.2022.2050887

Zhang, J.-L., Tasan, C. C., Lai, M. J., Yan, D., & Raabe, D. (2017). Partial recrystallization of gum metal to achieve enhanced strength and ductility. *Acta Materialia*, *135*, 400–410. https://doi.org/10.1016/j.actamat.2017.06.051